

# Quantitative evaluation of the impact of cloud transmittance and cloud velocity on the accuracy of short-term DNI forecasts



Mengying Li, Yinghao Chu, Hugo T.C. Pedro, Carlos F.M. Coimbra\*

Department of Mechanical and Aerospace Engineering, Jacobs School of Engineering, Center for Renewable Resource Integration, Center for Energy Research, University of California, San Diego, 9500 Gilman Drive, La Jolla, CA 92093, USA

## ARTICLE INFO

### Article history:

Received 13 June 2015

Received in revised form

24 September 2015

Accepted 26 September 2015

### Keywords:

Local sensing

Sky and cloud transmittances

Cloud velocity derivations

Solar forecasts

## ABSTRACT

Ground based sky imaging and irradiance sensors are used to quantitatively evaluate the impact of cloud transmittance and cloud velocity on the accuracy of short-term direct normal irradiance (DNI) forecasts. Eight representative partly-cloudy days are used as an evaluation dataset. Results show that incorporating real-time sky and cloud transmittances as inputs reduces the root mean square error (RMSE) of forecasts of both the Deterministic model (Det) (16.3%–17.8% reduction) and the multi-layer perceptron network model (MLP) (0.8% ~ 6.2% reduction). Four computer vision methods: the particle image velocimetry method, the optical flow method, the x-correlation method and the scale-invariant feature transform method have accuracies of 83.9%, 83.5%, 79.2% and 60.9% in deriving cloud velocity, with respect to manual detection. Analysis also shows that the cloud velocity has significant impact on the accuracy of DNI forecasts: underestimating the cloud velocity magnitude by 50% results in 30.2% (Det) and 24.2% (MLP) increase of forecast RMSE; a 50% overestimate results in 7.0% (Det) and 8.4% (MLP) increase of RMSE; a  $\pm 30^\circ$  deviation of cloud velocity direction increases the forecast RMSE by 6.2% (Det) and 6.6% (MLP).

© 2015 Elsevier Ltd. All rights reserved.

## 1. Introduction

The uncertainty in ground level solar irradiance caused by aerosols and clouds adversely affects the stability of solar power generation and therefore significantly increases the cost to balance generation and demand in real time [1–3]. High-fidelity short-term solar forecast technologies are beneficial to power plant operations, grid balancing, real-time unit dispatching, automatic generation control and power trading [1,4]. Therefore, they provide low-cost strategies to mitigate the intermittency of solar power and to decrease the solar energy integration cost.

Different short-term solar forecast methods have been developed to meet the increasing demands for solar integration [1,5–14]. Since the short-term variability of the solar irradiance at the ground level is mostly caused by cloud cover [15], either remote-sensing or local-sensing techniques are used to provide cloud information as inputs to forecasting models. Remote-sensing based models [16,17] use satellite images with limited temporal resolutions are not appropriate for short-term forecasts [12,18,19]. Therefore, local-

sensing based models that provide high resolution sky images are used for short-term forecasts with improved forecasting results compared to models with no exogenous inputs [12–14,20,21]. The derived cloud information consists of cloud cover, cloud transmittance and cloud velocity, which are usually computed by detecting clouds from sky images, analyzing lagged irradiance measurements and comparing consecutive sky images, respectively. However, the impact of the accuracy of cloud transmittance and velocity derivations from local sensing techniques on the accuracy of short-term solar irradiance forecasts has not been quantitatively studied.

In this work, we quantitatively evaluate the impact of cloud transmittance and cloud velocity on the accuracy of short-term direct normal irradiance (DNI) forecasts. We firstly assess DNI forecasts using manually detected cloud velocity with invariant and real-time sky and cloud transmittances inputs. This is done by visually comparing two consecutive sky images and measuring the displacement of clouds from the first image to the second image using e-ruler. With this information we manually compute cloud speed and moving direction. Forecast results are quantified in terms of mean bias error (MBE), mean absolute error (MAE), and root mean square error (RMSE). Then we evaluate the accuracies of

\* Corresponding author.

E-mail address: [ccoimbra@ucsd.edu](mailto:ccoimbra@ucsd.edu) (C.F.M. Coimbra).

four cloud velocity derivation methods by comparing their derived cloud velocities with manual detections. The four methods are Scale-invariant feature transform (SIFT), Optical flow (OF), X-correlation (X-corr), and Particle image velocimetry (PIV). The DNI forecast results based on the four methods are also calculated and analyzed. Finally, we quantitatively analyze the effect of cloud velocity uncertainty on the accuracy of DNI forecasts.

## 2. Preparation of data set

Broadband DNI was collected using a Rotating Shadowband Radiometer (RSR-2, manufactured by Irradiance, Inc). In Folsom, California (latitude = 38.64°, longitude = -121.14°), sky images are captured by a fish-eye camera (FE8174V, manufactured by Vivotek) installed next to the RSR-2. The fish-eye camera has a 180° field-of-view lens and a 3.1 MP CMOS sensor that captures and transfers sky images (via FTP) to a remote server once per minute and stores them in a MySQL database. The fish-eye camera is maintained locally and we manually discard sky images compromised by extensive soiling. Abnormal peaks and negative values in the DNI measurements and measurements when solar elevation angle is below 20° are discarded as well. DNI measurements are also examined randomly by comparing with corresponding sky images to ensure the precision of measurements and the synchronization between DNI data and the sky images.

Simultaneous irradiance data and sky images are downloaded from the MySQL database and paired as data points. During clear and overcast periods, the DNI is not affected by cloud cover. Therefore, we selectively study partly-cloudy periods from eight days of 2013 that include all types of clouds: March 16th (10:15 ~ 15:30), March 30th (8:40 ~ 11:20 and 14:10 ~ 15:45), April 1st (8:35 ~ 15:50), April 5th (9:40 ~ 15:50), April 6th (13:20 ~ 15:55), July 10th (13:00 ~ 16:00), July 22nd (8:00 ~ 16:00), July 23rd (8:00 ~ 9:20 and 11:05 ~ 14:25), yielding 2483 data points in total. The data set is randomly divided into a training set and a testing set for the stochastic multilayer perceptron network (MLP) model. The training set is two times bigger than the testing set, yielding 1862 data points in the training set and 621 data points in the testing set. Another scenario of data division is applied and compared to prevent the MLP model from over-training. The comparison results are presented in the Appendix. Cloud velocity is detected manually for each data point by comparing two adjacent sky images. The direction of cloud velocity is measured in unit of degree (°) starting from the east direction and increasing counterclockwise. Manually detected directions and magnitudes of cloud velocity have an uncertainty of ±20° and ±10 pixel/min, respectively.

## 3. Demonstration of methods

The methods demonstrated in this section are: (1) the cloud and sky transmittance derivation methods, (2) the cloud velocity derivation methods, (3) the cloud identification method that assists the cloud coverage determination for the DNI forecasting models, (4) the deterministic (Det) and the MLP DNI forecasting models which consider cloud transmittance and cloud velocity, and (5) the statistical metrics to assess the DNI forecasts.

### 3.1. Cloud and sky transmittances derivation methods

The cloud transmittance (CT) and sky transmittance (ST) are normally set to 0 and 1 in DNI forecasting models [12]. During clear periods, the presence of aerosols decreases the DNI and causes the clear period DNI to vary from day to day. Therefore, ST is often smaller than 1 due to aerosols. Compared to thick clouds, such as cumulonimbus, which absorb and reflect nearly all solar irradiance,

thin clouds, such as cirrus, only absorb and reflect a portion of it. Therefore, thin clouds have a CT greater than 0. To account for these phenomena, real-time CT and ST corrections are incorporated in this work. These are calculated as the mode of clear-sky indexes over the past 90 min [21,22], where the mode is defined as the number that is repeated more often than any other in a series and the clear-sky index is the irradiance value divided by the corresponding clear-sky irradiance,

$$CT(t) = \text{mode} \left( \frac{B}{B_{\text{clc}}} (t - 90 : t) < \theta_e \right) \quad (1)$$

$$ST(t) = \text{mode} \left( \frac{B}{B_{\text{clc}}} (t - 90 : t) > \theta_e \right) \quad (2)$$

where B is the actual DNI and  $B_{\text{clc}}$  is the clear-sky DNI calculated from the clear-sky model. An empirical clear-sky model is used to compute the clear-sky irradiance  $B_{\text{clc}}$  [14,19]. This model computes clear-sky DNI using an eighth-order polynomial expression that depends on the cosine of the solar elevation angle,

$$B_{\text{clc}} = \sum_{n=0}^8 a_n \cos^n \theta \quad (3)$$

The parameters of this polynomial expression are obtained using least square method for 30 selected clear-sky days. They are given as  $a_n = \{-0.01045, 5.898, -23.93, 58.79, -57.49, -50.98, 172.8, -146.9, 42.72\}$  [14,19]. This clear-sky model is simple and easy to implement and expected to have a higher accuracy than other DNI clear-sky models [19]. The threshold  $\theta_e$  is suggested to be 0.7 empirically [21], which assumes clouds have transmittances smaller than 0.7 while sky has a transmittance greater than 0.7 [23]. If no data over the past 90 min is available, CT is set to the default value 0 and ST is set to 1.

### 3.2. Cloud velocity derivation methods

Four cloud velocity derivation methods are analyzed: Scale invariant feature transform (SIFT), Optical flow (OF), X-correlation (X-corr), and Particle image velocimetry (PIV). A random method is used as a reference method.

The SIFT method is a computer vision method that extracts key points from a reference image [24,25]. These key points have specific features and are invariant to scaling, rotation or image translation. Key points with same features are recognized in a new image. Cloud velocities are derived by dividing the displacements between matched key points and the time interval between the two consecutive images. A representative cloud velocity is obtained using a k-means method [26].

The OF method has been widely used for computer vision applications [27] and has been recently introduced in the research of solar forecasts for cloud velocity derivation [28]. This method assumes that the brightness ( $I$ ) of an image pixel remains constant when it is displaced from location  $(x, y)$  at time  $t$  to another location  $(x + \Delta x, y + \Delta y)$  at time  $t + \Delta t$ , which results in  $I(x, y, t) = I(x + u\Delta t, y + v\Delta t, t + \Delta t)$ . To solve this equation for the  $u$  and  $v$  variables, additional constraints derived from several methods such as the correlation method, the gradient method or the regression method are needed. More details about the implementation of this method can be found in Refs. [28–30].

The X-corr method directly compares two consecutive images and computes the displacement that minimizes the matching errors using the Minimum quadratic difference method [31,32]. The representative cloud velocity is obtained by dividing the

displacement by the time interval between two consecutive images.

The PIV method analyzes two consecutive images and partitions each image into interrogation windows [12,19,33]. Cloud displacements are determined by analyzing the correlation between two consecutive interrogation windows using the Minimum quadratic difference method [34]. The velocities in all interrogation windows are obtained by dividing the cloud displacements by the time interval between the consecutive images and clustered using a k-means method to obtain a representative cloud velocity.

The random method is used as a reference to benchmark the cloud direction estimations by the above four methods. This method randomly generates a direction for the cloud velocity for each time point (no velocity magnitudes are generated).

### 3.3. Cloud identification methods

Cloud identification methods for sky images captured by the fish-eye cameras were developed by Chu et al. [15]. A smart adaptive cloud identification system (SACI) that integrates Fixed threshold method (FTM) [35], Minimum cross entropy method (MCE) [36–38] and Clear-sky library method (CSL) [18] was implemented and validated for a period of one month [15].

The SACI method categorizes each sky image as clear or cloudy using five criteria computed from past 10-min Global Horizontal Irradiance (GHI) time-series. The five criteria are mean GHI, max GHI, length of GHI time-series, variance of GHI, and maximum deviation from clear-sky gradient [39–41]. If an image is categorized as cloudy, the hybrid threshold method [35] is used to analyze the histograms for the red-channel to blue-channel ratio and further categorize the image as either overcast or partly-cloudy. After the image classification, the SACI employs FTM for overcast images, CSL with FTM for clear images, and CSL with MCE for partly-cloudy images. The SACI method is validated for various weather conditions and achieves over 90% accuracy [15]. Fig. 1(d)

illustrates an example of SACI cloud detection.

### 3.4. DNI forecasting models

The implementation of a deterministic DNI forecasting model (Det) and a multilayer perceptron network forecasting model (MLP) is discussed in this section.

#### 3.4.1. Deterministic forecasting model

Clouds that block the Sun significantly reduce the ground-level DNI and therefore are crucial for short-term solar forecasts. To identify the clouds with high relevance to future solar irradiance, a grid-cloud-fraction method was developed by Marquez and Coimbra to get numerical information about clouds that move towards the Sun [12].

The grid-cloud-fraction method can be summarized in five steps [12,19]:

1. Round sky images from fish-eye cameras are projected onto a flat square space to remove the geometric distortion (Fig. 1(b)).
2. The average velocity of the clouds is generated by the cloud velocity derivation methods (Section 3.2). The methods provide average cloud velocity in the sky (Fig. 1(c)).
3. The SACI is used to identify clouds from sky images to produce binary cloud maps (Section 3.3).
4. A set of grid elements ( $X_1, X_2, \dots, X_8$ ) is placed in the reverse direction of the cloud velocity from the Sun position on the binary cloud map (Fig. 1(d)). In this work, the area of grid elements is empirically set to 120 (length)  $\times$  120 (width) pixels.
5. The cloud indices  $Cl_p$  are computed as the fraction of pixels identified as cloud in grid element  $X_p$ .

The future values of the clear-sky index is expressed as:

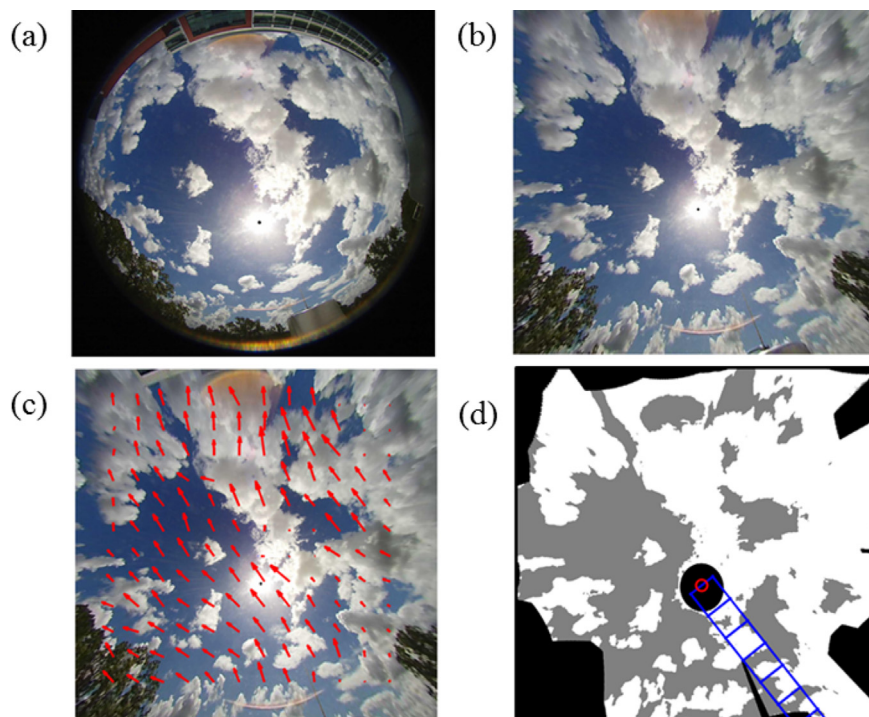


Fig. 1. Illustration of the grid-cloud-fraction method. The sky image was taken at 12:00pm on April 5th, 2013. The cloud velocity is derived from PIV method. The CI is computed for each square grid element.

$$k_{t,p}(t + FH) = \frac{\widehat{B}_p(t + FH)}{B_{\text{clc}}(t + FH)} = [\text{ST}(t)(1 - \text{Cl}_p(t)) + \text{Cl}_p(t) \cdot \text{CT}(t)] \quad (4)$$

where FH is the forecast horizon,  $\widehat{B}$  is the predicted DNI for future time, and ST and CT are the sky and cloud transmittance, respectively. Empirically,  $p = 3$  based on the forecast results in Ref. [12] and in this work.

### 3.4.2. MLP forecasting model

The multilayer perceptron neural network (MLP) is capable of forecasting arbitrary non-linear mappings [1,42] and is used to forecast DNI. The MLP consists of one input layer, several hidden layers and one output layer. Each hidden layer consists of several neurons – the processing elements. Chu et al. [15] optimized the structure of the MLP using a genetic algorithm [10,43,44]. As suggested by Chu et al. [15], an MLP structure with a single hidden layer containing 7 neurons is selected for this work. For a single hidden layer MLP, the data processing by each neuron on the hidden layer is [45]:

$$Y_i = f \left( \sum_{j=1}^J (w_{ij}X_j + \beta_{ij}) \right), \quad (5)$$

where  $Y_i$  is the output of the  $i$ -th neuron,  $f(\cdot)$  is the sigmoidal activation function  $f(z) = 1/(1 + \exp(-z))$ ,  $J$  is the number of inputs, and  $w_{ij}$  and  $\beta_{ij}$  are the weight and bias of the  $j$ -th input on the  $i$ -th neuron. The outputs from each neuron are then processed to generate the outputs of the MLP:

$$Z_k = f \left( \sum_{i=1}^I (w_{ki}Y_i + \beta_{ki}) \right), \quad (6)$$

where  $Z_k$  is the  $k$ -th output of the MLP,  $I$  is the number of neurons, and  $w_{ki}$  and  $\beta_{ki}$  are the weight and bias of the  $i$ -th neuron output on the  $k$ -th MLP output. The weights  $w_{ij}$ ,  $w_{ki}$ ,  $\beta_{ij}$  and  $\beta_{ki}$  are determined by a supervised learning process using the training data set. The weights are optimized to achieve minimum root mean square error (RMSE) between the MLP outputs  $\mathbf{Z}$  and the training targets  $\mathbf{Z}^I$ :

$$\text{MLP}_f = \text{argmin}_{\text{MLP}} \text{RMSE}(\mathbf{Z}, \mathbf{Z}^I). \quad (7)$$

The predictions from the trained MLP with new inputs are then:

$$\widehat{\mathbf{Z}} = \text{MLP}_f(\mathbf{X}^{\text{new}}). \quad (8)$$

The Bootstrap sampling method is implemented with the MLP to generate more accurate predictions. The Bootstrap method randomly samples the training set (with replacement) to generate  $N$  different training sets.  $N$  is set to 200 in this work as suggested by Carney et al. [46]. Then each of the  $n$ -th re-sampled sets is used to train an  $\text{MLP}_n$ . The ensemble prediction is thus the average of all  $N$  MLPs predictions:

$$\widehat{\mathbf{Z}} = \frac{1}{N} \sum_{n=1}^N \text{MLP}_n(\mathbf{X}^{\text{new}}). \quad (9)$$

Nine inputs are selected for the MLP model: the cloud indices  $\text{Cl}_2 \sim \text{Cl}_5$  (corresponding to the 2 ~ 5 grid elements) based on the direction of cloud velocity, the magnitude of cloud velocity  $|V|$ , the measured current clear-sky index  $k_t(t)$ , the sky transmittance ST, the cloud transmittance CT and the forecast horizon FH.

All the nine inputs are evaluated at the current time. The MLP

output is the predicted future clear-sky index  $\widehat{k}_t(t + \text{FH})$ .

### 3.5. Assessment metrics

We employ three statistical metrics to assess the accuracy of the DNI forecasts: mean biased error (MBE), mean absolute error (MAE) and root mean square error (RMSE).

$$\text{MBE} = \frac{1}{M} \sum_{m=1}^M (\widehat{B}(t_m) - B(t_m)) \quad (10)$$

$$\text{MAE} = \frac{1}{M} \sum_{m=1}^M \left| \widehat{B}(t_m) - B(t_m) \right| \quad (11)$$

$$\text{RMSE} = \sqrt{\frac{1}{M} \sum_{m=1}^M (\widehat{B}(t_m) - B(t_m))^2}, \quad (12)$$

where  $M$  is the number of data points in the testing set.

## 4. Results and discussion

### 4.1. Effect of the real-time cloud and sky transmittances

The effect of real-time sky and cloud transmittances on the accuracy of DNI forecasts is studied. Forecasts with invariant and real-time transmittances as inputs are compared and the results are presented in Table 1. Manually detected cloud velocity is used as input to the Det and MLP forecasting models to generate the 5-, 10- and 15-min ahead forecasts. When invariant transmittance is incorporated, the CT and ST in Eqs. (1) and (2) are set to be 0 and 1, respectively. The forecasting results are calculated using the testing data set.

#### 4.1.1. Deterministic model forecasts

The columns 9–11 of Table 1 show over 72.7% improvements on MBE, over 19.9% improvements on MAE and over 16.3% improvements on RMSE when real-time transmittances are incorporated to the Det model. Significant improvements of MBE indicate that incorporating real-time transmittances substantially reduces the negative bias in the DNI forecasts. Fig. 2 shows the histogram of the real-time ST and CT in our testing set. The presence of aerosols results in  $\text{ST} < 1$  for 82.2% of the testing period. For over 41.5% of the period tested, the ST equals to 0.90. Instances in which  $\text{CT} = 0$  (clouds absorb all solar irradiance) account for 46.7% of the period. For the remaining 53.3% of the testing period, CT ranges from 0.1 to 0.7.

Eq. (4) shows that DNI forecasts are an increasing function of the ST and CT. Therefore, compared with the invariant transmittances case ( $\text{ST} = 1$  and  $\text{CT} = 0$ ), when  $\text{CT} > 0$ , the DNI forecasts will increase while when  $\text{ST} < 1$ , the DNI forecasts will decrease. Since we selectively study partly-cloudy periods in this work, the DNI forecasts are mostly influenced by the CT rather than the ST. Therefore, the influence of increased CT outperforms the decreased ST, resulting in higher predicted values for DNI and higher MBE.

#### 4.1.2. MLP model forecasts

As presented in Table 1, incorporating real-time transmittances in the MLP model results in improvements over 19.4%, 2.2% and 0.8% for MBE, MAE and RMSE of the forecasts, respectively. The improvements of the MLP model are not as significant as the Det model because the stochastic MLP model can correct the transmittance information by adjusting the weights.

**Table 1**  
5-min, 10-min and 15-min ahead DNI forecast results.

FH (mins)		Invariant transmittances			Real-time transmittances			Improvements		
		MBE (W/m <sup>2</sup> )	MAE (W/m <sup>2</sup> )	RMSE (W/m <sup>2</sup> )	MBE (W/m <sup>2</sup> )	MAE (W/m <sup>2</sup> )	RMSE (W/m <sup>2</sup> )	ΔMBE (%)	ΔMAE (%)	ΔRMSE (%)
Det	5	-147.9	298.1	388.8	-40.4	235.3	325.3	72.7	21.0	16.3
	10	-144.5	294.0	385.9	-37.2	235.5	321.8	74.3	19.9	16.6
	15	-135.8	298.3	388.4	-28.7	235.0	319.2	78.9	21.2	17.8
MLP	5	-40.4	173.1	224.5	-22.9	169.3	222.7	43.3	2.2	0.8
	10	-43.2	182.0	234.2	-34.8	176.6	227.2	19.4	2.9	3.0
	15	-45.6	198.8	252.6	-28.8	188.2	236.8	36.8	5.3	6.2
Improvements of MLP over Det		Δ MBE (%)	ΔMAE (%)	ΔRMSE (%)	ΔMBE (%)	ΔMAE (%)	ΔRMSE (%)			
	5	72.7	41.9	42.3	43.3	28.1	31.5			
	10	70.1	38.1	39.3	6.4	25.0	29.4			
	15	66.4	33.4	35.0	-0.5	19.9	25.8			

The improvements of the MLP model over the Det model are presented in Table 1. The MLP forecasts outperform the Det forecasts in all metrics. When invariant transmittances are used, the improvements of MBE, MAE and RMSE are over 66.4%, 33.4% and 35.0%, respectively. When using real-time transmittances, the improvements are over -0.5%, 19.9% and 25.8% of MBE, MAE and

RMSE, respectively. The improvements of the MLP model over the Det model are larger with invariant transmittances than with real-time transmittances.

Fig. 3 plots the accumulated distributions of 10-min ahead forecasting errors of the Det and the MLP models with invariant and real-time transmittances. The Det model with real-time transmittances and the MLP model outperforms the Det model with invariant transmittances in the entire error range (0–900 W/m<sup>2</sup>). The Det model with real-time transmittances has more instances that fall in the small error range (0–80 W/m<sup>2</sup>) than the MLP model. The MLP model outperforms the Det model for the large error (80 W/m<sup>2</sup> - 900 W/m<sup>2</sup>). Therefore, the stochastic MLP model achieves lower MAE and RMSE than the Det model by reducing the large forecasting errors. Incorporating real-time transmittances in the MLP model only achieves limited improvements on the accuracy of forecasts.

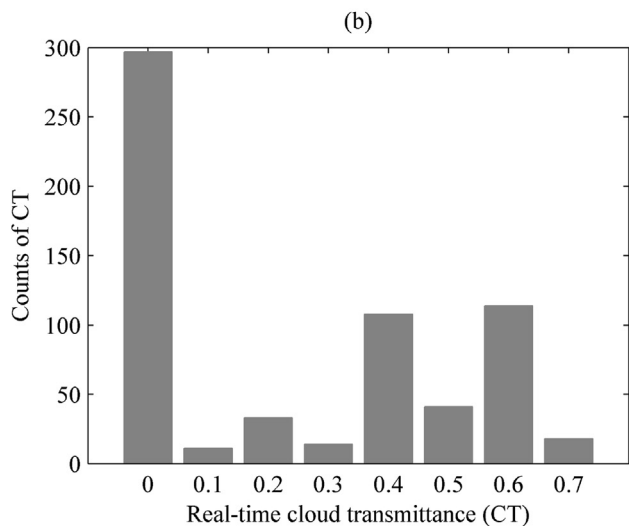
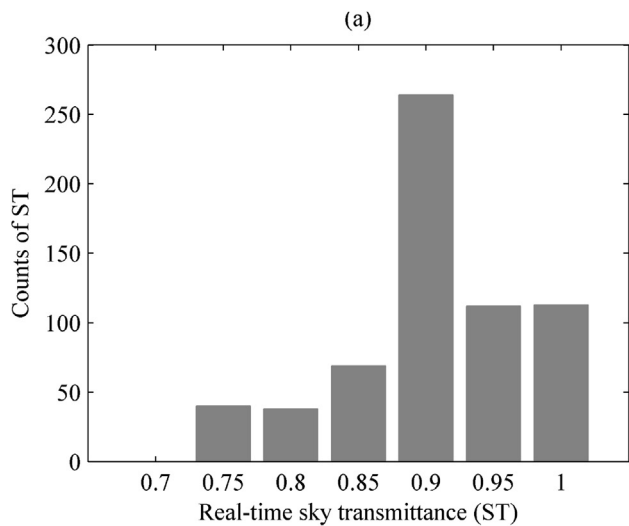


Fig. 2. Histogram of real-time ST and CT in the testing set.

4.2. Comparison of the cloud velocity derivation methods

The velocity derivation accuracies of SIFT, OF, X-corr and PIV methods are evaluated by comparing their derived cloud velocities with manually detected velocities. A velocity is deemed accurate if it is within the uncertainty ranges of manual detection, which are ±20° in direction and ±10 pixel/min in magnitude.

The sample time series of the derived cloud velocity are shown in Fig. 4. The measured clear-sky index, the derived velocity

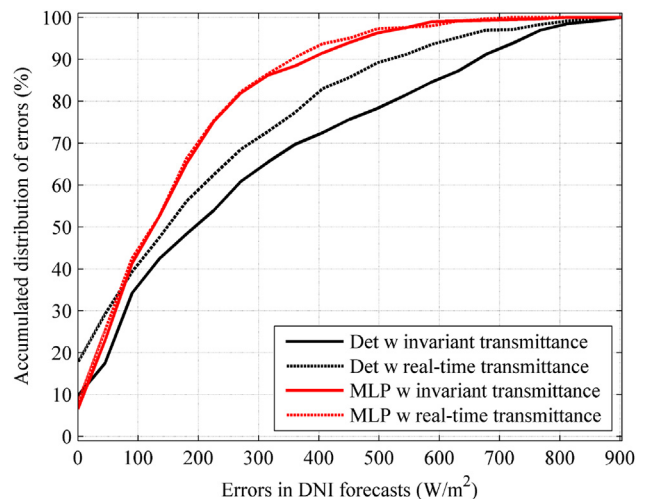


Fig. 3. Accumulated distribution of 10-min ahead DNI forecasting errors of the Det and the MLP models, with invariant and real-time transmittances.

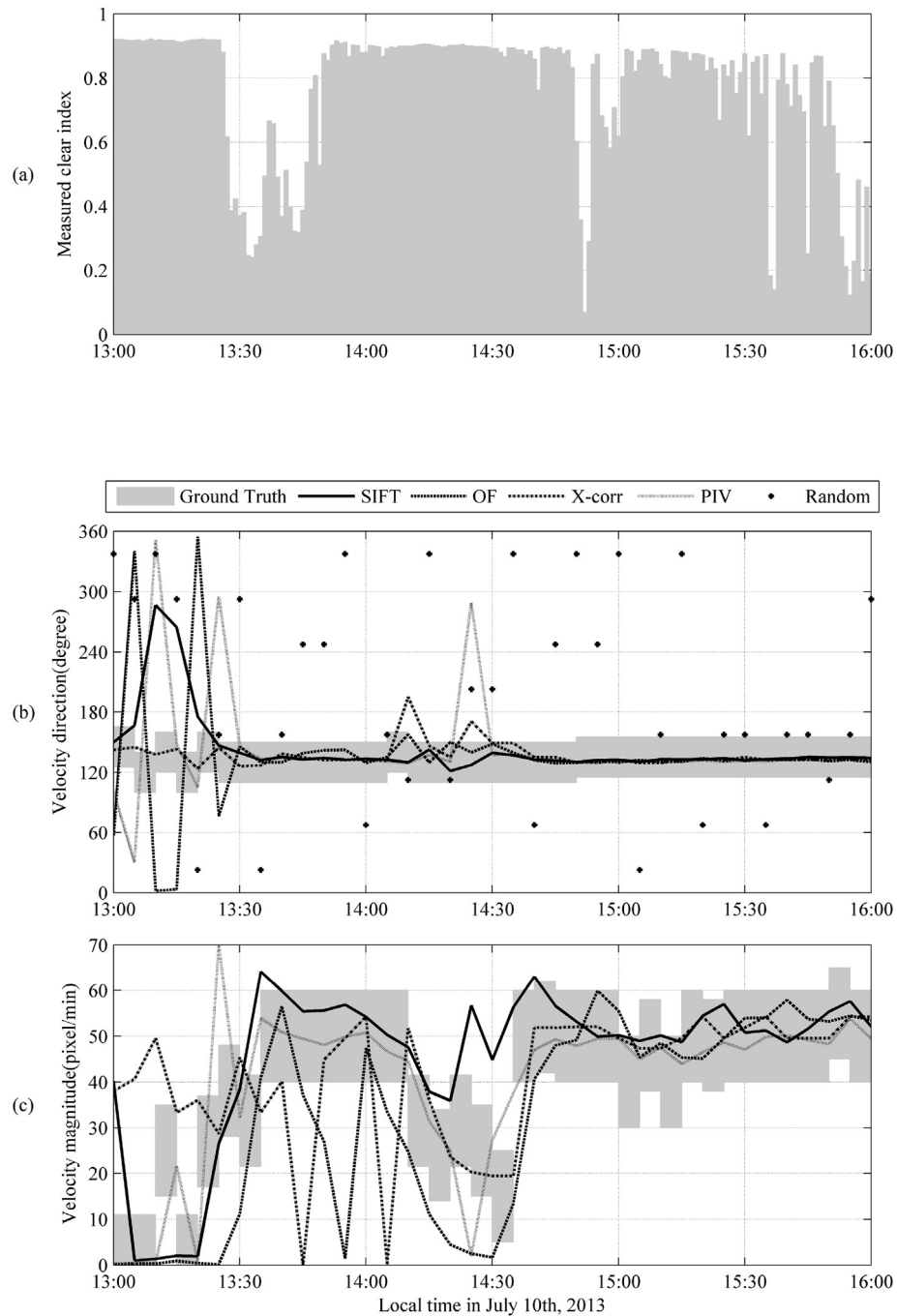


Fig. 4. Sample time series of the cloud velocity derived from representative methods.

direction and the derived velocity magnitude are plotted with respect to time in Fig. 4 (a), (b) and (c), respectively. All methods perform well during partly-cloudy periods (13:30 ~ 16:00). During clear period (13:00 ~ 13:30), the variation between two consecutive sky images is small. So the applied methods are unable to identify useful features to detect the cloud movements, resulting in large velocity derivation errors.

The accuracies of the cloud velocity derivation methods in the data set are presented in Table 2. PIV has the highest accuracy of 83.9%, followed by 83.5% for OF, 79.2% for X-corr and 60.9% for SIFT. The Random method has the lowest accuracy of only 7.6% (its accuracy is based on the direction of velocity only). The results of 10-

min ahead DNI forecasts using the cloud velocity derived from each method are presented in Table 2. The manually detected velocities are regarded as 'ground truth' and the corresponding DNI forecast results are listed as a reference.

The Pearson product moment correlation coefficients (Pearson-r) [47] between the accuracies of velocity derivations and the DNI forecast results are presented in Table 2 as well. When the accuracy of DNI forecasts is strongly correlated with the accuracies of cloud velocity, a negative correlation coefficient close to  $-1$  should be expected (more accurate velocity leads to more accurate DNI forecasts with smaller MBE, MAE and RMSE). The Pearson-r of MAE and RMSE of DNI forecasts are smaller than  $-0.45$  for the Det model

**Table 2**  
10-min ahead DNI forecast results using cloud velocity derived from representative methods.

Methods	Accuracy (%)	Invariant transmittances			Real-time transmittances			Improvements			
		MBE (W/m <sup>2</sup> )	MAE (W/m <sup>2</sup> )	RMSE (W/m <sup>2</sup> )	MBE (W/m <sup>2</sup> )	MAE (W/m <sup>2</sup> )	RMSE (W/m <sup>2</sup> )	ΔMBE (%)	ΔMAE (%)	ΔRMSE (%)	
Det	SIFT	60.9	-121.6	281.3	373.9	-23.6	222.3	309.1	80.6	21.0	17.3
	OF	83.5	-140.8	291.5	383.7	-35.1	233.4	321.0	75.1	20.0	16.3
	X-corr	79.2	-128.2	293.2	382.5	-27.7	240.3	325.3	78.4	18.1	15.0
	PIV	83.9	-131.3	283.3	377.2	-30.0	230.0	318.3	77.2	18.8	15.6
	Random	7.6	-90.0	301.3	396.5	-11.9	246.0	345.0	86.8	18.4	13.0
	Ground Truth	100.0	-144.5	294.0	385.9	-37.2	235.5	321.8	74.3	19.9	16.6
	Pearson-r		0.98	-0.45	-0.58	0.97	-0.45	-0.70			
MLP	SIFT	60.9	-40.1	191.0	243.6	-3.4	193.3	246.6	91.5	-1.2	-1.3
	OF	83.5	-51.7	192.7	242.7	-27.7	184.5	242.3	46.3	4.2	0.2
	X-corr	79.2	-38.0	191.7	248.1	-26.6	195.6	242.7	30.2	-2.0	2.2
	PIV	83.9	-28.5	183.4	233.6	-16.0	185.2	240.1	43.9	-1.0	-2.8
	Random	7.6	-46.5	213.3	276.9	71.4	211.8	288.1	-53.4	0.7	-4.0
	Ground Truth	100.0	-43.2	182.0	234.2	-34.8	176.6	227.2	19.4	2.9	3.0
	Pearson-r		-0.25	-0.95	-0.94	-0.65	-0.94	-0.99			

and smaller than -0.94 for the MLP model, indicating a strong correlation of the accuracy of DNI forecasts with the accuracy of cloud velocity. The Pearson-r is closer to -1 with the MLP model than with the Det model, indicating that the MLP model has a stronger dependence on the accurate cloud velocity inputs.

4.3. Effect of the cloud velocity on the DNI forecasts

The results from Table 2 are unable to identify the source of DNI forecast errors, i.e. the errors may result from the input cloud velocity uncertainty or are the baseline errors of the DNI forecasting models (Table 1). The Det and the MLP models with real-time transmittances are used to study the effect of cloud velocity on short-term DNI forecasts.

The baseline error of a DNI forecasting model is defined as the RMSE from the forecasting model when ‘ground truth’ cloud velocity is incorporated. The baseline forecast errors for 5-min, 10-min and 15-min ahead forecasts are presented in Table 1.

The increment of RMSE is calculated as the RMSE of forecasts when use inaccurate cloud velocity as input in the model minus the baseline error of the model,

$$\Delta RMSE = RMSE - RMSE_L \tag{13}$$

where the subscript L represents baseline error. Taking 10-min ahead forecasts as an example,  $RMSE_L = 321.8 \text{ W/m}^2$  for the Det model and  $RMSE_L = 227.2 \text{ W/m}^2$  for the MLP model (Table 1).

4.3.1. Deterministic model forecasts

The map of ΔRMSE caused by inaccurate cloud velocity input to the Det model is shown in Fig. 5. The radial coordinate represents the cloud indices  $Cl_p$  and the angular coordinate  $\theta$  represents the deviation of velocity direction from the ground truth. The ground truth cloud velocity is represented by  $\theta = 3^\circ$  and  $\theta = 0^\circ$  (denoted with a circle symbol on Fig. 5).

Incorporating ground truth cloud velocity direction,  $Cl_2$  (left cross symbol) indicates the cloud velocity magnitude is underestimated by 50%, because the cloud in the 2nd grid element will shade the Sun instead of the cloud in the 3rd grid element (Fig. 1(d)). Also  $Cl_4$  (right cross symbol) indicates the velocity magnitude is overestimated by 50%. Fig. 6 shows that a 50% underestimation of cloud velocity magnitude results in a 97.2 W/m<sup>2</sup> (30.2%) RMSE increase and a 50% overestimation results in a 22.6 W/m<sup>2</sup> (7.0%) RMSE increase.

Fig. 7 plots the ΔRMSE with respect to the deviation of velocity

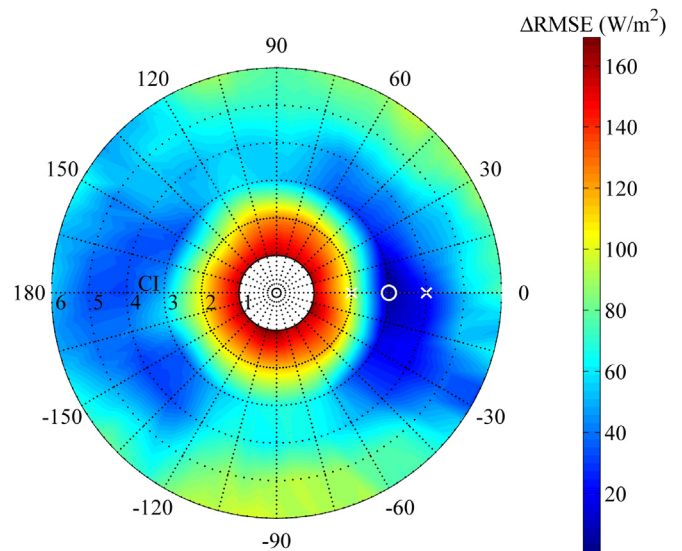


Fig. 5. The ΔRMSE of 10-min ahead forecasts from the Det model with respect to the deviations of cloud velocity from ground truth.

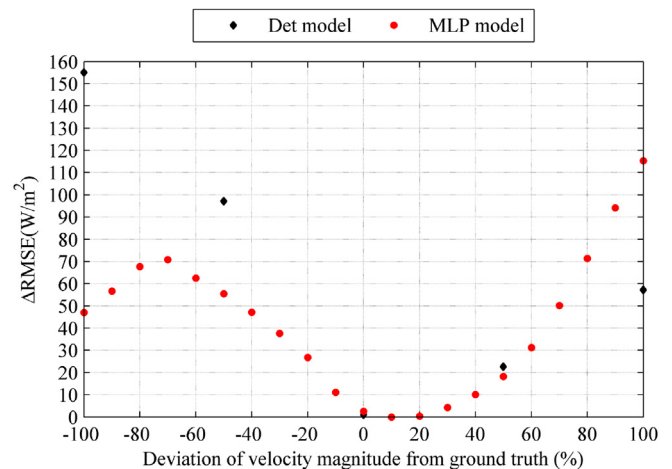


Fig. 6. ΔRMSE of the Det model and the MLP model with respect to the deviations of cloud velocity magnitude from ground truth.

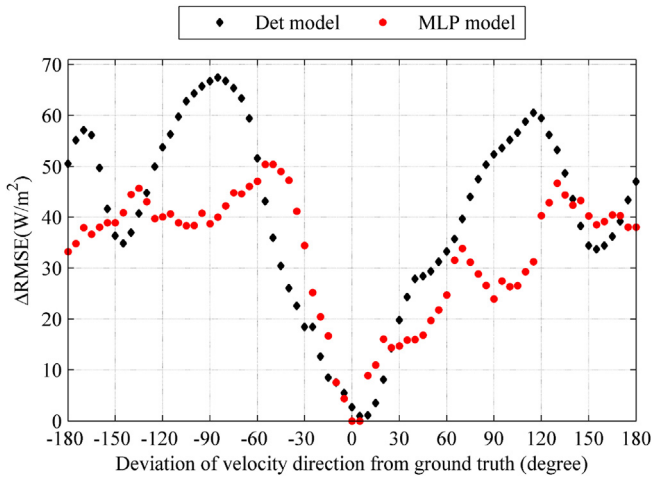


Fig. 7.  $\Delta$ RMSE of the Det model and the MLP model with respect to the deviations of cloud velocity direction from ground truth.

direction from ground truth at  $Cl_3$  (ground truth cloud velocity magnitude is used). The error in determining the cloud velocity direction can result up to a  $68 W/m^2$  (21.1%) RMSE increase. Smaller errors in velocity direction derivation can have a large impact. For instance, a  $\pm 30^\circ$  deviation increases the forecast RMSE by  $20 W/m^2$  (6.2%).

4.3.2. MLP model forecasts

Fig. 8 shows that the  $\Delta$ RMSE of the MLP model increases with respect to the deviations of both the cloud velocity magnitude and the direction from the ground truth.

To study the effect of cloud velocity magnitude, Fig. 6 plots the  $\Delta$ RMSE with respect to the derivation of velocity magnitude (ground truth cloud velocity direction is used). The error in determining the cloud velocity magnitude can result in a  $115 W/m^2$

(50.6%) RMSE increase. As seen in Fig. 4, the four methods used for deriving the cloud velocity tend to underestimate the cloud velocity magnitude. Underestimating the velocity magnitude by 50% increases the forecast RMSE by  $55 W/m^2$  (24.2%) while overestimating it by 50% increases the RMSE by  $19 W/m^2$  (8.4%).

To study the effect of cloud velocity direction, Fig. 7 shows the  $\Delta$ RMSE with respect to the derivation of velocity direction from ground truth (the ground truth velocity magnitude is used). The error in determining the cloud velocity direction can result in a  $50 W/m^2$  (22.0%) RMSE increase. Small errors such as a  $\pm 30^\circ$  deviation of cloud velocity direction increases the forecast RMSE by  $15 W/m^2$  (6.6%).

5. Conclusions

In this work, we analyze 5-, 10- and 15-min ahead DNI forecasts using a deterministic model (Det) and a Bootstrap multilayer perceptron network model (MLP). Both invariant and real-time sky and cloud transmittances are used as inputs for comparison. Cloud velocity uncertainty is also used as input to quantify the impact of velocity input on the DNI forecasts. Eight representative partly-cloudy days are selected as the data set.

Incorporating real-time transmittances in the Det model yields over 72.7%, 19.9% and 16.3% improvements of MBE, MAE and RMSE when compared to invariant transmittances. The improvements of the MLP model are over 19.4%, 2.2% and 0.8% of MBE, MAE and RMSE, respectively. With real-time transmittances inputs, the negative bias of the DNI forecasts is substantially reduced and the accuracies of both the Det and the MLP models are improved.

The accuracies of the four cloud velocity derivation methods and their correlations with forecast errors are analyzed. PIV is the most accurate and has an accuracy of 83.9% during the studied partly-cloudy periods. OF, X-corr and SIFT methods have 83.5%, 79.2% and 60.9% accuracies, respectively. The MAE and RMSE of 10-min ahead DNI forecasts are highly correlated with the accuracies of cloud velocity derivation. The Pearson correlation coefficients are

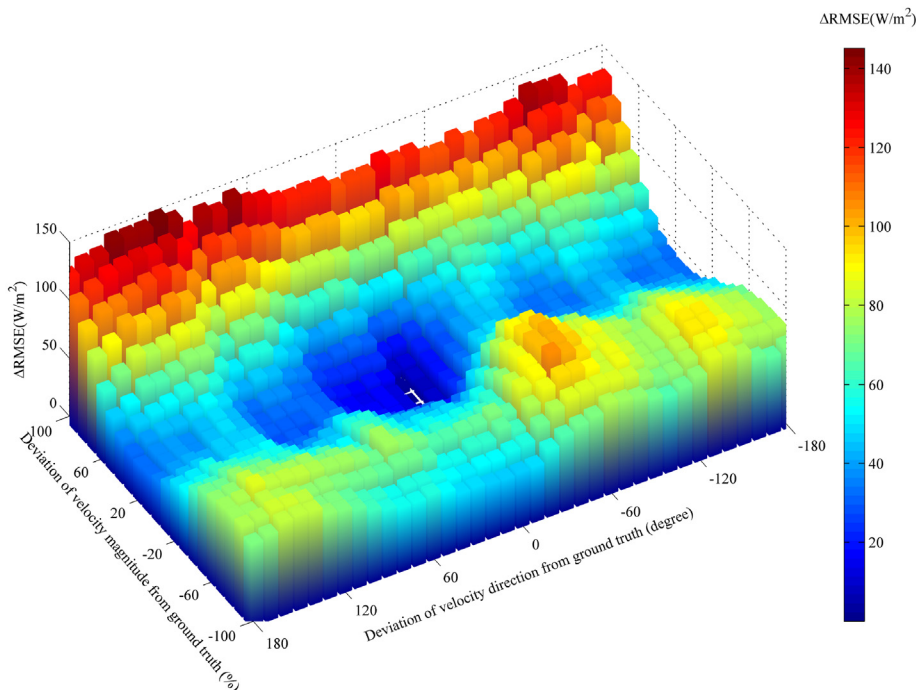


Fig. 8.  $\Delta$ RMSE with respect to the deviations of cloud velocity direction and magnitude from ground truth.

smaller than  $-0.45$  (Det) and  $-0.94$  (MLP).

The effect of cloud velocity on the accuracy of 10-min ahead DNI forecasts with real-time transmittances inputs is quantitatively evaluated using both the Det and the MLP model. A 50% underestimation of cloud velocity magnitude increases the forecast RMSE by 30.2% (Det) and 24.2% (MLP). A 50% overestimation results in a 7.0% (Det) and an 8.4% (MLP) increase. A  $\pm 30^\circ$  deviation of velocity direction increases the forecast RMSE by 6.2% (Det) and 6.6% (MLP).

In summary, this work quantifies the impact of cloud transmittance and cloud velocity on short-term DNI Forecasts. Both deviations in cloud velocity and invariant sky and cloud transmittances increase the errors of short-term DNI forecasts. It is recommended to incorporate real-time sky and cloud transmittances to the forecasting models and calibrate the cloud velocity derivations in order to increase forecast fidelity.

## Acknowledgments

The authors gratefully acknowledge the partial support by the California Energy Commission PIER PON-13-303 program, which is managed by Dr. Zhiqin Zhang. Ms. Zhouyi Liao helped in preparing the data set used in this work.

## Appendix

The dataset is randomly divided into a training set and a testing set to train the MLP model in this work. To justify the MLP results, another data sets dividing scenario using the beginning three-fourth of each day as training set and the rest of the day as testing set is compared. As seen in Table A1, the difference of two scenarios are less than 5.1% in terms of RMSE, indicating that our original MLP model did not over-trained.

**Table A1**  
5-min, 10-min and 15-min ahead DNI forecast results.

FH, min	Invariant transmittance			Historical transmittance		
	RMSE of MLP Original, W/m <sup>2</sup>	RMSE of MLP new, W/m <sup>2</sup>	Difference, %	RMSE of MLP Original, W/m <sup>2</sup>	RMSE of MLP new, W/m <sup>2</sup>	Difference, %
5	224.5	220.3	1.9	222.7	218.7	1.8
10	234.2	229.6	2.0	227.2	223.1	1.8
15	252.6	239.6	5.1	236.8	243.0	-2.6

## References

- [1] R.H. Inman, H.T.C. Pedro, C.F.M. Coimbra, Solar forecasting methods for renewable energy integration, *Prog. Energy Combust. Sci.* 39 (6) (2013) 535–576.
- [2] G.K. Singh, Solar power generation by PV (photovoltaic) technology: A review, *Energy* 53 (2013) 1–13.
- [3] Y. Chu, H.T.C. Pedro, M. Li, C.F.M. Coimbra, Real-time forecasting of solar irradiance ramps with smart image processing, *Sol. Energy* 114 (2015) 91–104.
- [4] D. Lew, R. Piwko, Western wind and solar integration study, Tech. rep., National Renewable Energy Laboratories, 2010. Technical Report No. NREL/SR-550-47781.
- [5] S.A. Kalogirou, Artificial neural networks in renewable energy systems applications: a review, *Renew. Sustain. energy Rev.* 5 (4) (2001) 373–401.
- [6] Y. Li, R. Luan, J. Niu, Forecast of power generation for grid-connected photovoltaic system based on grey model and Markov chain, in: ICIEA 2008 3rd IEEE Conference, 2008, pp. 1729–1733.
- [7] P. Bacher, H. Madsen, H.A. Nielsen, Online short-term solar power forecasting, *Sol. Energy* 83 (10) (2009) 1772–1783.
- [8] Y. Huang, J. Lu, C. Liu, X. Xu, W. Wang, X. Zhou, Comparative study of power forecasting methods for PV stations, in: Power System Technology (POWERCON), 2010 International Conference, IEEE, 2010, pp. 1–6.
- [9] M. Hassanzadeh, M. Etezadi-Amoli, M.S. Fadali, Practical approach for sub-

- hourly and hourly prediction of PV power output, in: In North American Power Symposium (NAPS), 2010, pp. 1–5.
- [10] R. Marquez, C.F.M. Coimbra, Forecasting of global and direct solar irradiance using stochastic learning methods, ground experiments and the NWS, database, *Sol. Energy* 85 (5) (2011) 746–756.
- [11] M. Lave, J. Kleissl, J.S. Stein, A wavelet-based variability model (WVM) for solar PV power plants, *IEEE Trans. Sustain. energy* 4 (2) (2012) 501–509.
- [12] R. Marquez, C.F.M. Coimbra, Intra-hour DNI forecasting methodology based on cloud tracking image analysis, *Sol. Energy* 91 (2013) 327–336.
- [13] R. Marquez, V.G. Gueorguiev, C.F.M. Coimbra, Forecasting of global horizontal irradiance using sky cover indices, *ASME J. Sol. Energy Eng.* 135 (2013) 0110171–0110175.
- [14] S. Quesada-Ruiz, Y. Chu, J. Tovar-Pescador, H.T.C. Pedro, C.F.M. Coimbra, Cloud-tracking methodology for intra-hour DNI forecasting, *Sol. Energy* 102 (2014) 267–275.
- [15] Y. Chu, H.T.C. Pedro, L. Nonnenmacher, R.H. Inman, Z. Liao, C.F.M. Coimbra, A smart image-based cloud detection system for intra-hour solar irradiance forecasts, *J. Atmos. Ocean. Technol.* 31 (2014) 1995–2007.
- [16] R. Perez, S. Kivalov, J. Schlemmer, K. Hemker, D. Renne, T.E. Hoff, Validation of short and medium term operational solar radiation forecasts in the US, *Sol. Energy* 84 (5) (2010) 2161–2172.
- [17] R. Marquez, H.T.C. Pedro, C.F.M. Coimbra, Hybrid solar forecasting method uses satellite imaging and ground telemetry as inputs to ANNs, *Sol. Energy* 92 (2013) 176–188.
- [18] M.S. Ghoniama, B. Urquhart, C.W. Chow, J.E. Shields, A. Cazorla, J. Kleissl, A method for cloud detection and opacity classification based on ground based sky imagery, *Atmos. Meas. Tech. Discuss.* 5 (2012) 4535–4569.
- [19] Y. Chu, H.T.C. Pedro, C.F.M. Coimbra, Hybrid intra-hour DNI forecasts with sky image processing enhanced by stochastic learning, *Sol. Energy* 98 (2013) 592–603.
- [20] C.W. Chow, B. Urquhart, M. Lave, A. Dominguez, J. Kleissl, J. Shields, B. Washom, Intra-hour forecasting with a total sky imager at the UC San Diego solar energy testbed, *Sol. Energy* 85 (11) (2011) 2881–2893.
- [21] B. Urquhart, M. Ghoniama, D. Nguyen, B. Kurtz, J. Kleissl, *Solar Energy Forecasting and Resource Assessment*, Elsevier, 2013.
- [22] B. Urquhart, C. W. Chow, D. Nguyen, J. Kleissl, M. Sengupta, J. Blatchford, D. Jeon, Towards intra-hour solar forecasting using two sky imagers at a large solar power plant, *Proceedings of the American Solar Energy Society*.
- [23] Y. Chu, B. Urquhart, S.M.I. Gohari, H.T.C. Pedro, J. Kleissl, C.F.M. Coimbra, Short-term reforecasting of power output from a 48 MWe solar PV plant, *Sol. Energy* 112 (2015) 68–77.
- [24] D. Lowe, Object recognition from local scale-invariant features, in: *Computer Vision, 1999. The Proceedings of the Seventh IEEE International Conference on vol. 2, 1999*, pp. 1150–1157.
- [25] M. Lourenço, J.P. Barreto, F. Vasconcelos, Srd-sift: Keypoint detection and matching in images with radial distortion, *Robotics, IEEE Trans* 28 (3) (2012) 752–760.
- [26] J.A. Hartigan, M.A. Wong, Algorithm AS 136: a k-means clustering algorithm, *Appl. Stat.* 28 (1979) 100–108.
- [27] Q. Wu, A correlation-relaxation-labeling framework for computing optical flow-template matching from a new perspective, *pattern analysis and machine intelligence, IEEE Trans.* 17 (9) (1995) 843–853.
- [28] L. Nonnenmacher, C.F.M. Coimbra, Streamline-based method for intra-day solar forecasting through remote sensing, *Sol. Energy* 108 (2014) 447–459.
- [29] B. Horn, B. Schunck, Determining optical flow, *Artif. Intell.* 17 (1981) 185–203.
- [30] D. Sun, S. Roth, M. Black, Secrets of optical flow estimation and their principles, in: *Computer Vision and Pattern Recognition (CVPR), 2010 IEEE Conference on, 2010*, pp. 2432–2439.
- [31] C. Thompson, L. Shure, *Image Processing Toolbox: For Use with MATLAB; [user's Guide]*, MathWorks, 1995.
- [32] L. Gui, W. Merzkirch, A method of tracking ensembles of particle images, *Exp. Fluids* 21 (6) (1996) 465–468.
- [33] R.J. Adrian, J. Westerweel, *Particle Image Velocimetry*, Cambridge University Press, 2011.
- [34] N. Mori, K.A. Chang, *Introduction to MPIV, User Manual and Program, 2003* available online at: <http://sauron.civil.eng.osaka-cu.ac.jp/~mori/software/mpiv>.
- [35] Q. Li, W. Lu, J. Yang, A hybrid thresholding algorithm for cloud detection on ground-based color images, *J. Atmos. Ocean. Technol.* 28 (2011) 1286–1296.
- [36] N. Otsu, A threshold selection method from gray level histograms, *IEEE Trans. Syst. Man. Cybern.* 9 (1979) 62–66.
- [37] C.H. Li, C.K. Lee, Minimum cross entropy thresholding, *Pattern Recognit.* 26 (1993) 617–625.
- [38] C.H. Li, P.K.S. Tam, An iterative algorithm for minimum cross entropy thresholding, *Pattern Recognit. Lett.* 19 (1998) 771–776.
- [39] C.N. Long, T.P. Ackerman, Identification of clear skies from broadband pyranometer measurements and calculation of downwelling shortwave cloud effects, *J. Geophys. Res.* 105 (2000) 15609–15626.
- [40] S. Younes, T. Muneer, Clear-sky classification procedures and models using a worldwide database, *Appl. Energy* 84 (2007) 623–645.
- [41] M. J. Reno, C. W. Hansen, J. S. Stein, Global horizontal irradiance clear sky models: implementation and analysis, Sandia National Laboratories (SAND2012-2389).
- [42] Y. Chu, M. Li, H.T.C. Pedro, C.F.M. Coimbra, Real-time prediction intervals for intra-hour DNI forecasts, *Renew. Energy* 83 (2015) 234–244.

- [43] J.H. Holland, *Adaptation in Natural and Artificial Systems: an Introductory Analysis with Applications to Biology, Control and Artificial Intelligence*, MIT Press, 1992.
- [44] H.T.C. Pedro, C.F.M. Coimbra, Assessment of forecasting techniques for solar power production with no exogenous inputs, *Sol. Energy* 86 (7) (2012) 2017–2028.
- [45] A. Mellit, Artificial intelligence technique for modeling and forecasting of solar radiation data: a review, *Int. J. Artif. Intell. Soft Comput.* (2010) 52–76.
- [46] J.G. Carney, P. Cunningham, U. Bhagwan, Confidence and prediction intervals for neural network ensembles, in: *Neural Networks, 1999. IJCNN'99. International Joint Conference on vol. 2*, IEEE, 1999, pp. 1215–1218.
- [47] K. Pearson, Note on regression and inheritance in the case of two parents, *Proc. R. Soc. Lond.* 58 (347–352) (1895) 240–242.